 doi:10.20944/preprints202110.0179.v1

Article

Impact of Well Placement in the Fractured Geothermal Reservoirs Based on Available Discrete Fractured System

Saeed Mahmoodpour [1,*], Mrityunjay Singh [2,*], Kristian Bär [3] and Ingo Sass [4,5]

[1] Group of Geothermal Science and Technology, Institute of Applied Geosciences, Technische Universität Darmstadt; saeed.mahmoodpour@tu-darmstadt.de
[2] Group of Geothermal Science and Technology, Institute of Applied Geosciences, Technische Universität Darmstadt; mrityunjay.singh@tu-darmstadt.de
[3] Group of Geothermal Science and Technology, Institute of Applied Geosciences, Technische Universität Darmstadt; baer@geo.tu-darmstadt.de
[4] Group of Geothermal Science and Technology, Institute of Applied Geosciences, Technische Universität Darmstadt;
[5] Darmstadt Graduate School of Excellence Energy Science and Engineering, Technische Universität Darmstadt; sass@geo.tu-darmstadt.de
* Correspondence: saeed.mahmoodpour@tu-darmstadt.de; mrityunjay.singh@tu-darmstadt.de

Abstract: Well placement optimization in a given geological setting for a fractured geothermal reservoir is a prerequisite for enhanced geothermal operations. High computational cost associated in the framework of fully coupled thermo-hydraulic-mechanical (THM) processes in a fractured reservoir simulation, makes the well positioning as a missing point in developing a field scale investigation. Here, in this study, we shed light on this topic through examining different injection-production well (doublet) position in a given real fracture network. Water and CO_2 are used as working fluids for geothermal operations and importance of well positions are examined using coupled THM numerical simulations for both the fluids. Results of this study are examined through the thermal breakthrough time, mass flux and the energy extraction potential to assess the impact of well position in a two-dimensional reservoir framework. Almost ten times of the difference between the final amount of heat extraction is observed for different well position but with the same well spacing and geological characteristics. Furthermore, stress field is be a strong function of well position that is important with respect to the possibility of unwanted stress development. As part of the MEET project, this study recommends to perform similar well placement optimization study for each fracture set in a fully coupled THM manner before a field well drilling.

Keywords: Well placement; CO_2-EGS; water-EGS; Discrete fracture networks; THM modeling

1. Introduction

Geothermal field development and management is a complex process. Engineering a geothermal system requires appropriate well placement and fracture connectivity to ensure well connectivity and least fluid loss [1]. Placement of injection and production wells or a doublet system in a given geological uncertainty to achieve maximum geothermal energy extraction is one of the most complicated and expensive procedure. The location of injection well with respect to production wells decides the production mass flux [2]. Practically, there are infinite number of locations where an injection well can be placed in designing an enhanced geothermal system (EGS). Well placement in association with fracture network requires two key aspects in order to ensure high heat extraction potential: first, the fractures must be connected sufficiently and they must ensure high fluid flow rate at a low-pressure difference and the secondly, the fluid residence time in the fractures should be high to allow sufficient heat exchange. Longer residence time enhances the heat extraction capacity and reduces the chances of short-circuiting [3,4]. Figure 1 shows a fracture network in the subsurface where red color is the high temperature region. Cold water is injected through the blue color well and hot water is produced using the red colored

Preprints (www.preprints.org) | NOT PEER-REVIEWED | Posted: 12 October 2021 doi:10.20944/preprints202110.0179.v1

well. Fractures are the main flow paths for fluid flow that allow for the heat extraction from the various MEET geothermal sites including Soultz sous Forets, United Down, Göttingen and Havelange. DFN characterization is an important step toward the simulation of the reservoir performance. In other side, the output of the DFN would be a high number of fractures which is not feasible (from computational costs) to use all of them discretely through the thermal- hydraulic (TH) or thermal-hydraulic-mechanical (THM) simulator. At the same time, the fracture network alignment also contributes in the thermal drawdown, mass flux and the extracted energy. Therefore, it is essential to estimate the well locations a priori for better connectivity and the maximum energy extraction. In this paper, a two-dimensional fractured reservoir is considered for a potential enhanced geothermal system. Fully coupled thermo-hydro-mechanical (THM) processes are simulated on the fractured reservoir to estimate maximum geothermal energy extraction potential.

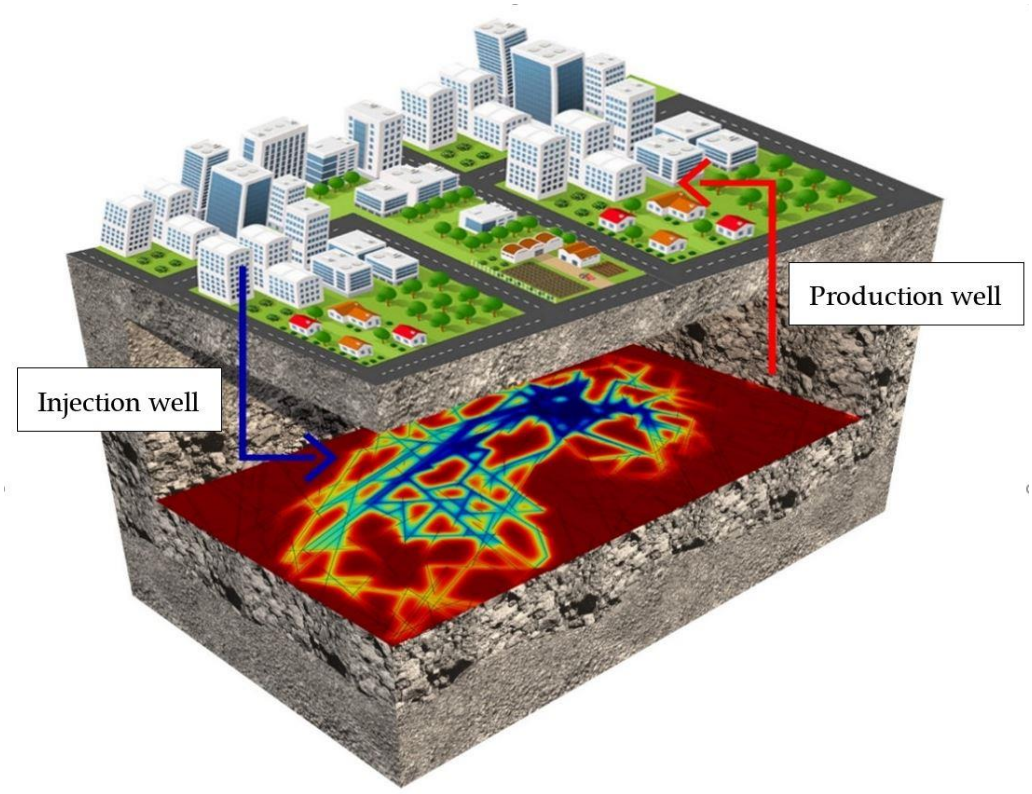

Figure 1. An enhanced geothermal system. The subsurface plan shows an intricate network of fractures. For optimized power generation, appropriate placement of the injection and production wells is necessary.

Several optimization techniques are available for determining well placement in a reservoir [5]. Some of these methods are gradient free methods including genetic algorithms, particle swarm optimization algorithm [6], fast marching method [7] and simultaneous perturbation stochastic approximation [8,9] and gradient based optimization methods including adjoint methods [10, 11, 12, 13]. These models lack in geological uncertainty while considering well placement optimization [14]. Very few thermo-hydraulic compositional reservoir simulation-based models are available on well spacing optimization [15, 16, 17, 18, 19]. Based on a coupled thermo-hydraulic model, Akin et al. [20] developed artificial neural networks (ANN) and a search algorithm to optimize an injection well for a geothermal reservoir whereas, Samin et al. [21] developed a hybrid approach integrating a multi-objective genetic algorithm with finite element modeling of thermo-hydraulic processes. EGS involves complex THM processes. Gudmundsdottir and Horne [22] developed an ANN model to characterize fractured geothermal reservoir for a coupled TH model. Training necessary data necessary for developing a robust ANN model based on

 doi:10.20944/preprints202110.0179.v1

a coupled thermo-hydro-mechanical process needs large number of numerical reservoir simulations. Recent study using an ANN model for a coupled thermo-hydraulic approach supports this idea for fracture hot geothermal [23, 24] and supercritical geothermal reservoirs [25].

While performing a parametric investigation for a multi-well reservoir, Chen and Jiang [26] found that production well configuration with respect to injection well affects the heat mining potential. Chen et al. [27] used a multivariate adaptive regression spline technique coupled with hydrothermal numerical simulation to optimize the well placement under the given fault size, and permeability for a prospective geothermal site near Superstition Mountain in Southern California, USA. They found that for the maximum net profit over a period of fifty years, the optimal well spacing is 473 m at 30.7 kg/s. For 45^{O} angle between fracture orientation and inlet-outlet connection in a given fracture network, Zhang et al. [28] observed optimized geothermal energy extraction performance. For higher orientation angles, they obtained stable heat mining rate at reduced efficiency. Zhang et al. [29] found that the presence of large number of fractures in vicinity of the production well increases the working fluid residence time and heat recovery efficiency significantly improves. They suggested that thermally-induced fractures near the production wells assists in greater power generation compared to when the fracture density is high in the vicinity of the injection well. They also observed that placing the production well in the high permeability region leads to higher thermal energy extraction. Gao et al. [30] used a coupled thermo-hydraulic model for a discrete fracture network in a fractured geothermal reservoir to investigate heat extraction performance. They used multilateral well orientations with varying number of branch wells and well orientation and found that with increase in the well and fracture intersections, production temperature decreases whereas injection pressure increases. Aliyu et al. [31] and Aliyu and Chen [32] used COMSOL Multiphysics to develop a model depicting THM and TH processes in a geothermal reservoir for two fractures and single fracture, respectively. They estimated the impact of well spacing on the thermal energy extraction performance.

The above literature show that there is no available THM model for determining an optimized location for the well placement to maximize mass flux, energy extraction and the thermal drawdown duration. In this work, a fully coupled THM model is developed and used to optimize the well position by characterizing the fracture network connectivity and density. The present study is organized in the following manner: first a mathematical and numerical model is presented for a coupled THM process followed by results and discussion on optimizing well positions in a two-dimensional fracture network based on thermal drawdown, mass flux and energy extraction potential followed by conclusions.

2. Methodology

A fracture network based on outcrop fractures mapped from Otsego County in New York state [33] is used for THM modeling in this study. The reservoir geometry is a two-dimensional planar model (1000 m × 600 m) and the injection-production wells are placed 500 m apart. An initial case is considered where injection well is present at point 0 and the production well is present at point 180 as shown in Figure 2. Considering this axis as diameter, a circular zone is assumed and the perimeter is divided into 36 equal intervals. These 36 intervals are considered for placing the injection and production wells and they are arranged at α angle from the base case. All fractures are assumed as interior boundaries and the displacement is constrained in all normal directions. The side boundaries are assumed as no flow for both heat and mass exchange.

Preprints (www.preprints.org) | NOT PEER-REVIEWED | Posted: 12 October 2021 doi:10.20944/preprints202110.0179.v1

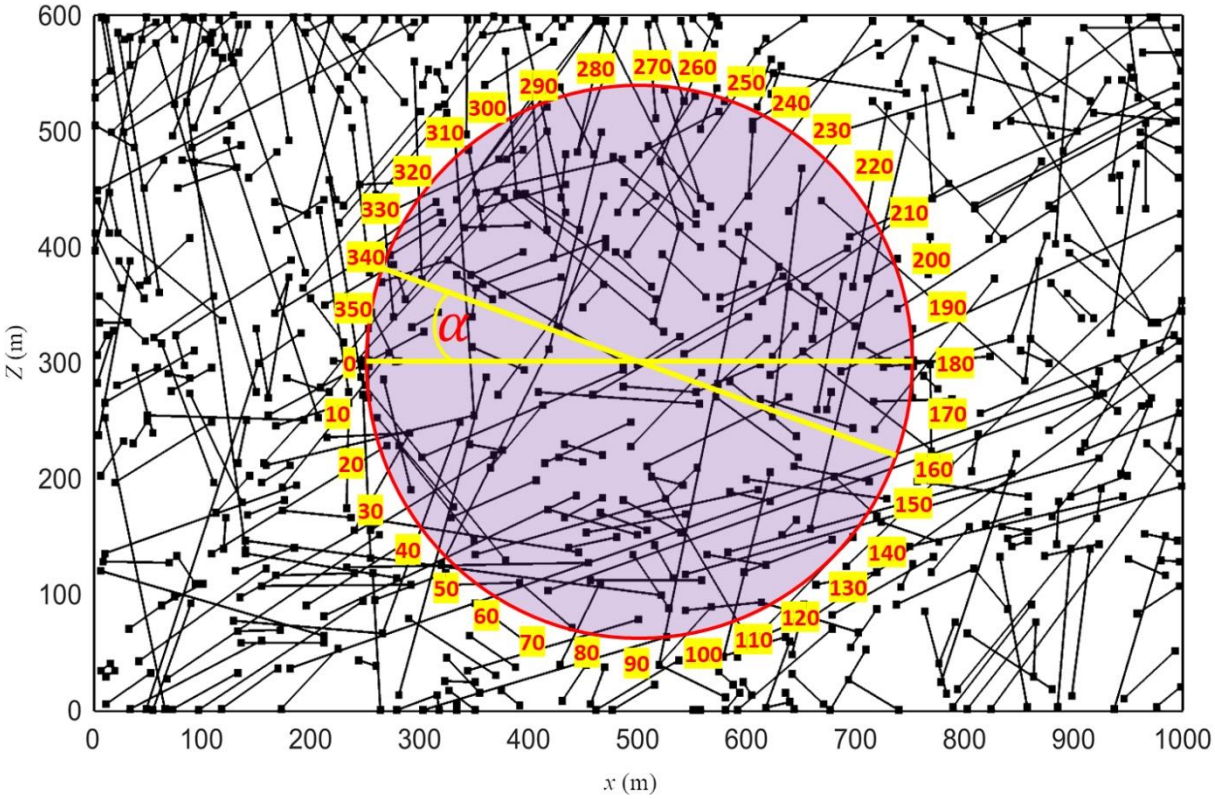

Figure 2. Geometry of the reservoir. Injection and production wells are placed 500 m apart. Total 36 cases or 36 values of α are considered for simulations. For example, when the injection well is present at 0 and production well is present at 180 and they are 500 m placed apart. The well orientation is the angle α measured for the location of injection well with respect to the case 0 - 180.

Conservation equation of mass when coupled with pore volume and fluid temperature alteration for a porous medium is:

$$\boldsymbol{\rho_1(\phi_m S_1 + (1-\phi_m)S_m)\frac{\partial p}{\partial t} - \rho_1(\alpha_m(\phi_m\beta_1 + (1-\phi_m)\beta_m))\frac{\partial T}{\partial t} + \rho_1\alpha_m\frac{\partial \varepsilon_V}{\partial t} = \nabla.(\frac{\rho_1 k_m}{\mu}\nabla p)} \quad [1]$$

All the parameters are listed in the Appendix: Table A1. Water and supercritical CO_2 are considered as heat transmitting fluids in this study. The equation governing fluid flow along the internal fractures is:

$$\boldsymbol{\rho_1(\phi_f S_1 + (1-\phi_f)S_{mf})e_h\frac{\partial p}{\partial t} - \rho_1(\alpha_f(\phi_f\beta_1 + (1-\phi_f)\beta_f))e_h\frac{\partial T}{\partial t} + \rho_1\alpha_f e_h\frac{\partial \varepsilon_V}{\partial t} = \nabla_T.\left(\frac{e_h\rho_1 k_f}{\mu}\nabla_T p\right) + n.Q_m} \quad [2]$$

In the above equation, fluid flow along the fracture width is ignored due to the fact that fracture aperture is much smaller compared to the fracture length. Fractures and the rock matrix are assumed at thermodynamic inequilibrium. In other words, local thermal non-equilibrium model is implemented in this investigation.

$$\boldsymbol{(1-\phi_m)\rho_m C_{p,m}\frac{\partial T_m}{\partial t} = \nabla.\left((1-\phi_m)\lambda_m\nabla T_m\right) + q_{ml}(T_l - T_m)} \quad [3]$$

$$\boldsymbol{(1-\phi_f)e_h\rho_f C_{p,f}\frac{\partial T_m}{\partial t} = \nabla_T.\left((1-\phi_f)e_h\lambda_f\nabla_T T_m\right) + e_h q_{fl}(T_l - T_m) + n.(-(1-\phi_m)\lambda_m\nabla T_m)} \quad [4]$$

Energy balance equation for the rock matrix and fractures are shown by Eq. [3] and Eq. [4] respectively. The energy balance equation for either water or CO_2 is:

$$\boldsymbol{\phi_m\rho_l C_{p,l}\frac{\partial T_l}{\partial t} + \phi_m\rho_l C_{p,l}(-\frac{k_m\nabla p}{\mu}).\nabla T_l = \nabla.(\phi_m\lambda_l\nabla T_l) + q_{ml}(T_m - T_l)} \quad [5]$$

Heat exchange between rock and the fracture matrix can be written by the following equation:

$$\boldsymbol{\phi_f e_h\rho_l C_{p,l}\frac{\partial T_l}{\partial t} + \phi_f e_h\rho_l C_{p,l}(-\frac{k_f\nabla_T p}{\mu}).\nabla_T T_l = \nabla_T.\left(\phi_f e_h\lambda_l\nabla_T T_l\right) + e_h q_{fl}(T_m - T_l) + n.(-\phi_l\lambda_l\nabla T_l)} \quad [6]$$

Preprints (www.preprints.org) | NOT PEER-REVIEWED | Posted: 12 October 2021 doi:10.20944/preprints202110.0179.v1

In the above equation, the Darcy flux in the fractures is $\boldsymbol{u_f} = -\frac{\boldsymbol{k_f \nabla_T p}}{\boldsymbol{\mu}}$ and heat flux is $\boldsymbol{n.q_l} = \boldsymbol{n}.(-\boldsymbol{\phi_l \lambda_l \nabla T_l})$. Thermodynamic properties of water and CO_2 represented by Eq. [10 - 17] and they are implemented in Eq. [1 - 6].

A fully coupled thermo-hydro-mechanical model is developed in this study. If the effective stress is $\boldsymbol{\sigma_{eff}^{ij}} = \boldsymbol{\sigma_{ij}} + \boldsymbol{\alpha_p p \delta_{ij}}$ and the volumetrix expansion coefficient of porous media is $\boldsymbol{\beta_T} = \boldsymbol{\phi_l \beta_l} + (\boldsymbol{1} - \boldsymbol{\phi_m})\boldsymbol{\beta_m}$, then the stress-strain relationship considering fully coupled thermoelastic and poroelastic stress can be written as:

$$\boldsymbol{\sigma_{ij}} = \boldsymbol{2G\varepsilon_{ij}} + \boldsymbol{\lambda tr\varepsilon \delta_{ij}} - \boldsymbol{\alpha_p p \delta_{ij}} - \boldsymbol{K'\beta_T T \delta_{ij}} \quad [7]$$

The reservoir deformation equation can be written as:

$$\boldsymbol{Gu_{i,jj}} + (\boldsymbol{G} + \boldsymbol{\lambda})\boldsymbol{u_{j,ji}} - \boldsymbol{\alpha_p p_{,i}} - \boldsymbol{K'\beta_T T_{,i}} + \boldsymbol{f_i} = \boldsymbol{0} \quad [8]$$

The opening and closure of the thermo-poroelastic stress-dependent fracture aperture are modeled using the Barton and Bandis model [34, 35] as follow:

$$\Delta \boldsymbol{e_n} = \frac{\boldsymbol{e_0}}{\boldsymbol{1+9\frac{\sigma_{eff}^{n}}{\sigma_{nref}}}} \quad [9]$$

In the above equation, $\Delta \boldsymbol{e_n}$ is the fracture aperture change under in-situ stress condition.

The thermophysical properties of water and CO_2 such as dynamic viscosity (Eq. [10, 11]), specific heat capacity (Eq. [12, 13]), density (Eq. [14, 15]), and thermal conductivity (Eq. [16, 17]) as a function of temperature are written below:

$$\boldsymbol{\mu_w} = \boldsymbol{1.38 - 2.12 \times 10^{-2} \times T^1 + 1.36 \times 10^{-4} \times T^2 - 4.65 \times 10^{-7} \times T^3 + 8.90 \times 10^{-10} \times T^4 - 9.08 \times 10^{-13} \times T^5 + 3.85 \times 10^{-16} \times T^6} \quad (\boldsymbol{273.15 - 413.15\ K}) \quad [10]$$

$$\boldsymbol{\mu_{CO_2}} = \boldsymbol{-1.49 \times 10^{-6} - 6.47 \times 10^{-8} \times T^1 - 3.66 \times 10^{-11} \times T^2 + 1.25 \times 10^{-14} \times T^3} \quad (\boldsymbol{220 - 600\ K}) \quad [11]$$

$$\boldsymbol{C_{p,w}} = \boldsymbol{1.20 \times 10^4 - 8.04 \times 10^1 \times T^1 + 3.10 \times 10^{-1} \times T^2 - 5.38 \times 10^{-4} \times T^3 + 3.63 \times 10^{-7} \times T^4} \quad [12]$$

$$\boldsymbol{C_{p,CO_2}} = \boldsymbol{459.91 + 1.86 \times T^1 - 2.13 \times 10^{-3} \times T^2 + 1.22 \times 10^{-6} \times T^3} \quad (\boldsymbol{220 - 600\ K}) \quad [13]$$

$$\boldsymbol{\rho_w} = \boldsymbol{1.03 \times 10^{-5} \times T^3 - 1.34 \times 10^{-2} \times T^2 + 4.97 \times T + 4.32 \times 10^2} \quad [14]$$

$$\boldsymbol{\rho_{CO_2}} = \boldsymbol{pA \times 0.04401/RT} \quad [15]$$

$$\boldsymbol{\kappa_w} = \boldsymbol{-8.69 \times 10^{-1} + 8.95 \times 10^{-3} \times T^1 - 1.58 \times 10^{-5} \times T^2 + 7.98 \times 10^{-9} \times T^3} \quad [16]$$

$$\boldsymbol{\kappa_{CO_2}} = \boldsymbol{-1.32 \times 10^{-3} + 4.14 \times 10^{-5} \times T^1 + 6.71 \times 10^{-8} \times T^2 - 2.11 \times 10^{-11} \times T^3} \quad [17]$$

In Eq. [15], $\boldsymbol{pA}$ is the absolute pressure and $\boldsymbol{R}$ is the molar gas constant.

COMSOL Multiphysics version 5.5 [36] is used to perform numerical modeling of THM processes. It uses a finte element method to solve general purpose partial differential equations. The complete mesh contains 112, 818 domain elements and 13,071 boundary elements. For the numerical modeling purpose, we have used an scaled absolute tolerance of magnitude 10^{-8} and automatic time step constraint. We assumed Backward Differentiation Formula (BDF) for timestepping with maximum BDF order as 2 and minimum BDF order as 1. Further, we have validated our model with a soil thermal consolidation model as demonstrated by Bai [37] in Mahmoodpour et al. [38].

Preprints (www.preprints.org) | NOT PEER-REVIEWED | Posted: 12 October 2021 doi:10.20944/preprints202110.0179.v1

Table 1. Numerical simulation parameters.

Symbol	Parameter	Magnitude for water based simulations	Magnitude for CO_2 based simulations
E	Young's modulus	40 GPa	40 GPa
ν	Poisson's ratio	0.25	0.25
ϱr	Rock density	$2500\ \frac{kg}{m^3}$	$2500\ \frac{kg}{m^3}$
S1	Horizontal stress	50 MPa	50 MPa
S2	Vertical stress	50 MPa	50 MPa
pi	Initial pressure	30 MPa	30 MPa
pj	Injection pressure	50 MPa	50 MPa
ϕr	Rock porosity	0.2	0.2
kr	Rock permeability	2 mD	5 mD
ϕf	Fracture zone porosity	0.5	0.5
f	Fracture roughness	1	1
Ap	Fracture aperture	0.2 mm	0.2 mm
σs	Closure stress	150 MPa	150 MPa
wr	Wellbore radius	0.2 m	0.2 m
λr	Rock thermal conductivity	$3\ \frac{W}{m \times K}$	$3\ \frac{W}{m \times K}$
λf	Fracture zone thermal conductivity	$2.5\frac{W}{m \times K}$	$2.5\frac{W}{m \times K}$
Cr	Rock specific heat capacity	$800\frac{J}{kg \times K}$	$800\frac{J}{kg \times K}$
Cf	Fracture zone specific heat capacity	$800\frac{J}{kg \times K}$	$800\frac{J}{kg \times K}$
Ti	Initial temperature	200 °C	200 °C
α	Biot coefficient	0.7	0.7
β	Thermal expansion coefficient	$10^{-5}\frac{1}{K}$	$10^{-5}\frac{1}{K}$
Tj	Injection temperature	70 °C	70 °C

3. Results and Discussions

Numerical simulation results from coupled THM mechanisms associated with a geothermal energy extraction process from a fractured reservoir are presented in this section. The adopted sequence of presentation is following: (a) coupled THM mechanisms for heat mining using water as heat carrying fluid, (b) coupled THM processes when CO_2 is the heat carrying fluid, and (c) predicting the suitable doublet well position for a given fracture network to obtain highest mass flux from the production well and maximize the heat production.

Figure 3 shows time evolution of reservoir temperature distribution during the heat extraction operation using water and CO_2 for case 180. Here, the injection well is present at 180 and production well is present at 0 as indicated in Figure 2. The reservoir permeability for the left (Figure 3a1-d1) and right (Figure 3a3-d3) columns is 5 mD whereas the middle column has 2 mD permeability. Higher reservoir permeability in the case of left column causes faster cold fluid propagation through the fracture network. Also, water propagation through the fractures becomes less dominant and it starts flowing through the rock matrix at higher permeability as shown in the Figure 3(c1 & d1), we adopted less reservoir permeability for well placement optimization when water is the working fluid. The cold-water propagation is aligned along the dominant fracture rather than horizontal axis between the doublet.

Preprints (www.preprints.org) | NOT PEER-REVIEWED | Posted: 12 October 2021 doi:10.20944/preprints202110.0179.v1

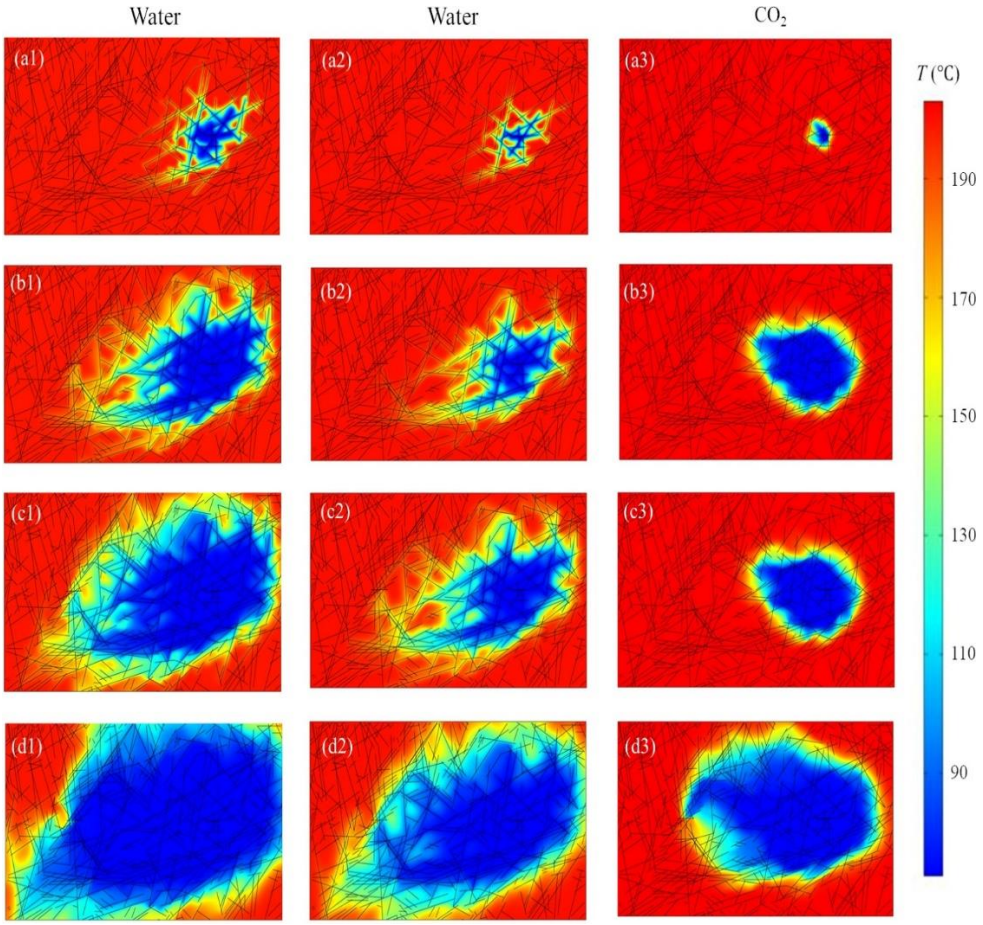

Figure 3. Reservoir temperature distribution at time 1 year (a1, a2 & a3), 5 years (b1, b2 & b3), 10 years (c1, c2 & c3) and 30 years (d1, d2 & d3) when the injection well is present at 180 and the production well is placed at 0. Results from water for reservoir permeability 5 mD and 2 mD are shown by (a1, b1, c1 & d1) and (a2, b2, c2 & d2) respectively. CO_2 as working fluid results are displayed in (a3, b3, c3 & d3). The reservoir permeability for CO2 simulations is 5 mD.

Viscosity of supercritical CO_2 at injection conditions is approximately half compared to water. Higher reservoir permeability and lower viscosity results in the injected CO_2 to propagates through the fractures as well as through the matrix rather than flowing through fractures only as seen in Figure 3(a2 & b2). From Figure 3(a3 - d3) it is clearly visible that the cold fluid plume spread is much diffusive manner compared to water and flow is primarily occurring through the matrix. However, Figure 3(d3) shows that near the production well, CO_2 flows through the dominant fractures. Therefore, the propagation of fluid through the fractures is the principal mechanisms between the doublet which is assisted by flow through permeable rock matrix.

Results obtained from the 36 reservoir simulations on the well positioning are shown in Figure 4. For water simulations, reservoir permeability is taken as 2 mD whereas for cases with CO_2 as working fluid, permeability is 5 mD. Water based models demonstrate faster thermal breakthrough due to higher specific heat capacity compared to CO_2 and therefore, water simulations are presented till 30 years whereas CO_2 results are plotted till 300 years. Figure 4(a) shows thermal drawdown at the production well when water is the working fluid. The fastest thermal drawdown in observed for case 220 (see Figure 5c1) whereas slowest thermal drawdown has occurred for case 130 (see Figure 5a1). From Figure 2, it is clear that case 220 has well position along a dominant fracture supported by small intersecting fractures whereas case 130 wells are aligned approximately orthogonal to this dominant fracture. Figure 5(a2) shows thermoelastic stress along the horizontal direction and it indicates stress localization is spanning across the cold fluid plume region. Greater concentration of connected fractures in the region away from the doublet axis

Preprints (www.preprints.org) | NOT PEER-REVIEWED | Posted: 12 October 2021 doi:10.20944/preprints202110.0179.v1

causes extremely slow thermal breakthrough time. Therefore, in 30 years, temperature drop is approximately 40 ℃ for case 130 whereas case 220 shows 75 ℃ temperature drop at the production well. In comparison to water, CO_2 has approximately seven times smaller thermal conductivity at the injection conditions. Due to this, thermal depletion time is very slow when CO_2 is the working fluid compared to water as the heat carrying fluid. Figure 4(b) shows the thermal drawdown at the production well when CO_2 is the working fluid and it shows that the thermal drawdown curves depends significantly on the fracture network connectivity than water. The slowest thermal drawdown is shown by case 40 where production well temperature drops by approximately 20 ℃ in 300 years whereas the fastest thermal drawdown in displayed by case 180 where approximately 90 ℃ temperature drop is estimated. Figure 6(a1) and 6(a2) shows reservoir temperature distribution for case 40 and case 180 respectively. In Figure 6(a1), the cold fluid spread is extremely slow due to the fact that a high fracture density is present near the point 40 as shown in Figure 2 that is present away from the doublet axis. This leads to reduced amount of cold fluid injection and restricted heat exchange between the fluid – fractures and fluid – matrix in the reservoir which subsequently decreases the horizontal and vertical thermoelastic stress as shown in Figure 6(a2) and 6(a3) respectively. Our numerical simulations consider poroelastic stress but we have not shown here as they contribute little due to the fluid injection and production as shown in our previous findings [38,39]. For the case 180, Figure 6(b1) shows reservoir temperature distribution after 300 years and it indicates that the hot fluid has been completely extracted between the doublet and the heat replenishment is too slow to recharge this depleting heat content. Figure 6(b2 & b3) approves this reasoning that due to favorable fracture density along the doublet axis, higher fluid injection assists in developing higher thermoelastic stress development.

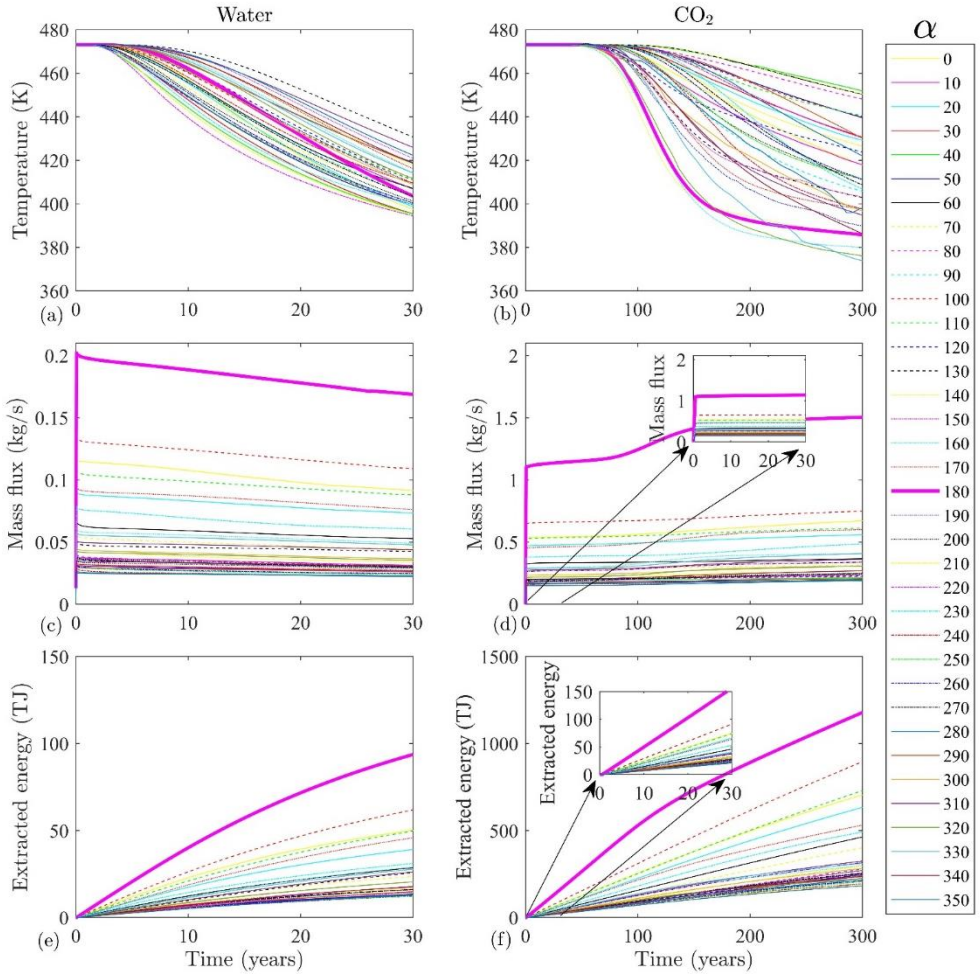

 doi:10.20944/preprints202110.0179.v1

Figure 4: Temperature at the production well for (a) water and (b) CO_2, mass flux at the production well for (c) water and (d) CO_2, and energy extracted using (e) water and (f) CO_2 as heat carrying fluid. Here Case 0 means injection well is present at 0 and production well is present at 180.

Figure 4(c) and 4(d) shows mass flux at the production well for 36 cases when the working fluid in the reservoir is water and CO_2, respectively. The mass flux for CO_2 is approximately five times higher than water to compensate the effect of smaller viscosity by maintaining the reservoir injection pressure. For both the fluids highest mass flux is observed for case 180 and smallest mass flux is observed for case 350. Even though these two doublet arrangements have approximately same axis, the fracture density near the production well plays the crucial role in mass flux. For case 180, fractures are well connected near the production well which assist in higher fluid production whereas in case of 350, fractures are not connected in a wide area leading to smaller fluid production. This can be easily seen from the stress distribution plots in Figure 5(e2 & e3) for case 350 when water is the working fluid and in Figure 6(c2 & c3) for case 350 when CO_2 is the heat transfer fluid. The decrease in mass flux for all the cases with time is due to decrease in water viscosity with increase in fluid temperature. However, we observe that the mass flux increases with time if CO_2 is the working fluid. This increase is approximately < 30% between the period when CO_2 production starts till 300 years of numerical simulation. This increase is pronounced for the case 180 where we observe that the mass flux increases from 1.15 to 1.5 kg/s and the increase starts after approximately 50 years from the beginning of the operation. This discrepancy is observed due to limitation in the equation of state used in modeling using COMSOL Multiphysics.

Preprints (www.preprints.org) | NOT PEER-REVIEWED | Posted: 12 October 2021 doi:10.20944/preprints202110.0179.v1

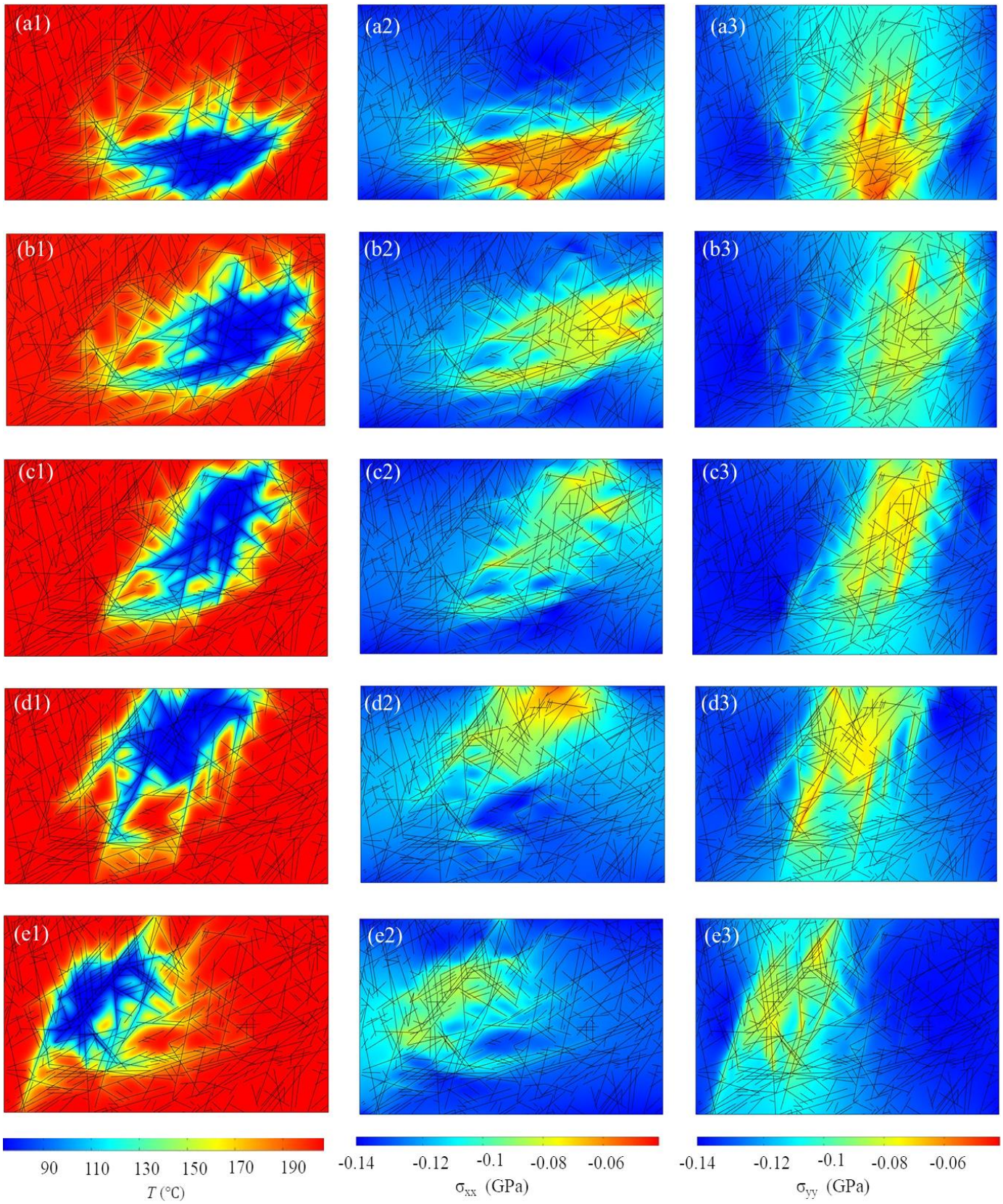

Figure 5. Distribution of (a1, b1, c1, d1 & e1) reservoir temperature, (a2, b2, c2, d2 & e2) horizontal thermoelastic stress and (a3, b3, c3, d3 & e3) vertical thermoelastic stress when water is used as the working fluid. Here Case 130 is displayed by (a1, a2 & a3), Case 180 is displayed by (b1, b2 & b3), Case 220 is displayed by (c1, c2 & c3), Case 250 is displayed by (d1, d2 & d3), and Case 350 is displayed by (e1, e2 & e3). All contours are plotted at 10 years.

Preprints (www.preprints.org) | NOT PEER-REVIEWED | Posted: 12 October 2021 doi:10.20944/preprints202110.0179.v1

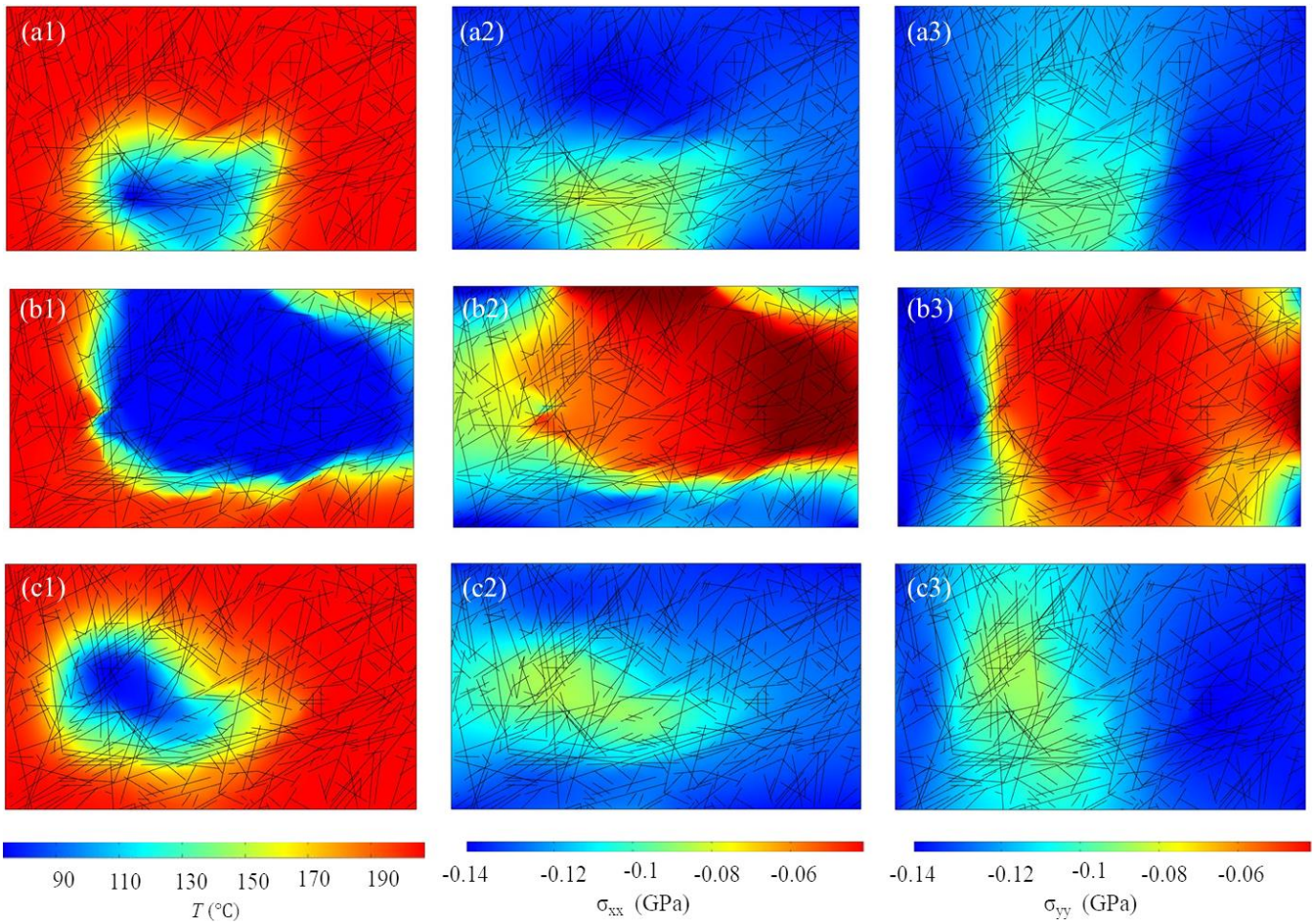

Figure 6. Distribution of (a1, b1 & c1) reservoir temperature, (a2, b2 & c2) horizontal thermoelastic stress and (a3, b3 & c3) vertical thermoelastic stress when CO_2 is used as the working fluid. Here Case 40 is displayed by (a1, a2 & a3), Case 180 is displayed by (b1, b2 & b3), Case 350 is displayed by (c1, c2 & c3). All contours are plotted at 100 years.

The energy extraction potential from the reservoir for both the fluids are approximately same due to the fact that in case of water simulations, reservoir permeability is 2.5 times smaller compared to CO_2 and mass flux of CO_2 is approximately 3-5 times greater than water whereas the specific heat capacity of water is approximately 3 times higher compared to CO_2 with 3 times higher viscosity. Due to higher mass flux and delayed thermal drawdown operation, total energy extraction potential is significantly higher when CO_2 is the working fluid. Case 180 for both the fluids show highest energy extraction potential due to maximum mass flow rate as shown in Figure 5(b1, b2 & b3). However, due to higher mass flux, thermal depletion is also fastest and therefore, doublet placed for case 180 may not show a longer operation when water is the working fluid. Case 250 for water and case 350 for CO_2 show least energy extraction potential over a period of 30 and 300 years respectively. Figure 5(d1) show the reservoir temperature distribution for case 250 and water is the used for heat transmission. It is clearly visible from the Figure 5(d1) that a greater amount of cold fluid is present near the injection well and there is only one large fracture along the doublet axis. This limits the fluid transmission at higher rate only through a narrow region causing limited energy extraction. On the other hand, Figure 6(c1) show reservoir temperature distribution for case 350 and CO_2 is used as working fluid and localization of cold fluid near the injection well in absence of any dominating fracture system, the passage of fluid is limited through the fractures toward the production well. However, since thermal breakthrough is much slow when CO_2 is used for heat transmission, energy extraction potential may enhance if EGS operation is performed beyond 300 years.

Preprints (www.preprints.org) | NOT PEER-REVIEWED | Posted: 12 October 2021 doi:10.20944/preprints202110.0179.v1

5. Conclusions

Geothermal energy extraction from deep fractured reservoirs can support high energy demand for a long duration. Water and CO_2 are two fluids that can be used for extracting energy from the subsurface. Fractured reservoir shows a complex network of fractures and fracture conductivity controls the main fluid passage for heat extraction longevity of the operation. Well placement for a given fracture network should consider the fracture density and fracture orientation. Keeping all the parameters constant, only the orientation of the injection – production doublet axis, we observe a difference of approximately ten times of energy extracted among the studied cases. As it affects the injectivity (poroelastic stress) and temperature propagation (thermoelastic stress), it has a great impact on the stress field development during the heat extraction.

Fluid type plays a significant role in determining the THM behavior of the EGS. Viscosity of fluid determines the temperature propagation through the fractures as well as through the rock matrix. CO_2 with lower viscosity can penetrate easily inside the matrix zone. This effect combine with the lower specific heat capacity of CO_2 eventuates the process of cold front of fluid propagation through the matrix and fracture. While water with the high viscosity and specific heat capacity, mainly transmit heat alongside the fracture and result in early breakthrough time. Different cases with water have a small range of breakthrough time compared to CO_2. While CO_2 shows a higher flow rate, resulting from the lower viscosity, however this behavior is compensated by higher heat capacity of water and therefore, the overall heat extraction is comparable for both the fluids.

Author Contributions: Conceptualization, S. Mahmoodpour and M. Singh.; methodology, S. Mahmoodpour and M. Singh.; software, S. Mahmoodpour and M. Singh; validation, S. Mahmoodpour and M. Singh writing—original draft preparation, S. Mahmoodpour and M. Singh; writing—review and editing, K. Bär.; visualization, S. Mahmoodpour and M. Singh; supervision, K- Bär and I. Sass; project administration, K. Bär; funding acquisition, K.Bär. All authors have read and agreed to the published version of the manuscript.

Funding: The work is conducted as part of the MEET project that has received funding from the European Union's Horizon 2020 research and innovation programme under grant agreement No 792037.

Data Availability Statement: Data used in this paper are synthetic and can be reproduced from the Table 1.

Acknowledgments: Group of Geothermal Science and Technology, Institute of Applied Geosciences, Technische Universität Darmstadt has provided institutional support to authors.

Conflicts of Interest: The authors declare no conflict of interest.

Appendix A

Table A1. List of parameters.

Symbol	Parameter
p	Fluid pressure
T	Fluid Temperature
ε_v	Pore volumetric strain
α_m	Biot's coefficient of porous media
α_f	Biot's coefficient of the fracture
ϕ_m	Reservoir porosity
ϕ_f	Fracture zone porosity
S_m	Storage coefficients of fluid
S_1	Storage coefficients of rock matrix
S_f	Storage coefficients of fracture
β_1	Thermal expansion coefficients of fluid
β_m	Thermal expansion coefficients of rock matrix
β_f	Thermal expansion coefficient of fracture
ρ & ρ_1	Fluid density
k_m	pressure-dependent rock matrix permeability

Preprints (www.preprints.org) | NOT PEER-REVIEWED | Posted: 12 October 2021 doi:10.20944/preprints202110.0179.v1

k_f	stress-dependent fracture permeability
e_h	hydraulic aperture between two fracture surfaces
nQ_m	$n.(-\frac{\rho k_m}{\mu \nabla p})$, mass flux exchange between porous media and the fracture
∇_T	Gradient operator restricted to the fracture's tangential plane
T_m	Rock matrix temperature
T_l	Fluid temperature
ρ_m	Rock density
$C_{p,m}$	Specific heat capacity of the rock matrix
λ_m	Heat conductivity of the rock matrix
q_{ml}	Rock matrix-pore fluid interface heat transfer coefficient
ρ_f	density of the fracture zone
$C_{p,f}$	Specific heat capacity of the fracture
λ_f	Heat conductivity of the fracture
q_{fl}	Rock fracture-fluid interface heat transfer coefficient
C_p & $C_{p,l}$	Heat capacity of the fluid at a constant pressure
λ_l	Heat conductivity of the fluid
σ_{ij}	Total stress
G & λ	Lame's constants
tr	Trace operator
K'	$\frac{2G(1+\nu)}{3(1-2\nu)}$, bulk modulus of the drained porous media
β_T	Volumetric thermal expansion coefficient of porous media
δ_{ij}	Dirac dealt function
α_p	Biot's coefficient
σ_{eff}^{ij}	Effective stress
f_i	External body force
Δe_n	Change in the initial aperture of the fracture under in-situ stresses
e_0	Initial aperture of the fracture
σ_{eff}^{n}	Effective normal stress acting on the fracture surface
σ_{nref}	Effective normal stress required to cause 90% reduction in fracture aperture
μ	CO_2 dynamic viscosity
κ	CO_2 thermal conductivity

References

1. Akin, S., Kok, M.V., Uraz, I., "Optimization of well placement geothermal reservoirs using artificial intelligence", Computers & Geosciences, 2010, 36, 776-785.
2. Aliyu, M.D., Chen, H.-P., "Optimum control parameters and long-term productivity of geothermal reservoirs using coupled thermo-hydraulic process modeling", Renewable Energy, 2017, 112, 151-165.
3. Aliyu, M.D., Chen, H.-P., Harireche, O., "Finite element modeling for productivity of geothermal reservoirs via extraction well", Proceedings of the 24th UK conference of the Association for Computational Mechanics in Engineering, 31 March-01 April 2016, Cardiff University, Cardiff, 331-334.
4. Ansari, E., Hughes, R., White, C.D., "Well placement optimization for maximum energy recovery from hot saline aquifers", Proceedings, Thirty-Ninth Workshop on Geothermal Reservoir Engineering, Stanford University, Stanford, California, February 24-26, 2014, SGP-TR-202.
5. Babaei, M., Nick, H.M., "Performance of low-enthalpy geothermal systems: Interplay of spatially correlated heterogeneity and well-doublet spacings", Applied Energy, 2019, 253, 113569.
6. Bai, B., "One-dimensional thermal consolidation characteristics of geotechnical media under non-isothermal condition", Eng. Mech., 22, p: 186-191, 2005.
7. Blank, L., Rioseco, E.M., Caiazzo, A., Wilbrandt, U., "Modeling, simulation, and optimization of geothermal energy production from hot sedimentary aquifers", Computational Geosciences, 2021, 25, 67-104.
8. Bandis, S, C., Lumsden, A, C., Barton, N, R., "Fundamentals of rock joint deformation", International Journal of Rock Mechanics and Mining Sciences & Geomechanics Abstracts, 20, 6, p:249-268, 1983.
9. Bangerth, W., Klie, H., Wheeler, M., Stoffa, P., Sen, M., "On optimization algorithms for the reservoir oil well placement problem", Comput. Geosci., 2006, 10, 303–319.
10. Barton, N., Bandis, S., Bakhtar, K., "Strength, deformation and conductivity coupling of rock joints", International Journal of Rock Mechanics and Mining Sciences & Geomechanics Abstracts, 22, 3, p: 121-140, 1985.
11. Chen, J., Jiang, F., "Designing multi-well layout for enhanced geothermal system to better 489 exploit hot dry rock geothermal energy", Renewable Energy, 2015, 74, 37-48.
12. Chen, M., Tompson, A.F.B., Mellors, R.J., Abdalla, "An efficient optimization of well placement and control for geothermal prospect under geological uncertainty", Applied Energy, 137, 2015, 352-363.

13. Chen, S.-Y., Hsieh, B.-Z., Hsu, K.-C., Chang, Y.-F., Liu, J.-W., Fan, K.-C., Chiang, L.-W., Han, Y.-L., "Well spacing of the doublet at the Huangtsuishan geothermal site, Taiwan", Geothermics, 2021, 89, 101968.
14. Forouzanfar, F., Li G., Reynolds, A.C., "A two-stage well placement optimization method based on adjoint gradient", in: SPE Annual Technical Conference and Exhibition, Florence, Italy, September 2010.
15. Gao, X., Zhang, Y., Huang, Y., Ma, Y., Zhao, Y., Liu, Q., "Study on heat extraction considering the number and orientation of multilateral wells in a complex fractured geothermal reservoir", Renewable Energy, 2021, 177, 833-852.
16. Gudmundsdottir, H., Horne, R.N., "Inferring interwell connectivity in fractured geothermal reservoirs using neural networks", Proceedings World Geothermal Congress, 2020+1, Reykjavik, Iceland, April-October 2021.
17. Hofmann, H., Babadagli, T., Yoon, J.S., Blöcher, G., Zimmermann, G., "A hybrid discrete/finite element modeling study of complex hydraulic fracture development for enhanced geothermal systems (EGS) in granitic basements", Geothermics, 2016, 64, 362–381.
18. Hofmann, H., Babadagli, T., Zimmermann, G., "Hot water generation for oil sands processing from enhanced geothermal systems: process simulation for different hydraulic fracturing scenarios", Appl. Energy, 2014, 113, 524–547.
19. Ishitsuka, K., Kobayashi, Y., Watanabe, N., Yamaya, Y., Bjarkson, E., Suzuki, A., Mogi, T., Asanuma, H., Kajiwara, T., Sugimoto, T., Saito, R., "Bayesian and neural network approached to estimate deep temperature distribution for assessing a supercritical geothermal system: Evaluation using a numerical model", Natural Resources Research, 2021, https://doi.org/10.1007/s11053-021-09874-w.
20. Islam, J., Vasant, P.M., Negash, B.M., Laruccia, M.B., Myint, M., Watada, "A holistic review on artificial intelligence techniques for well placement optimization problem", Advances in Engineering Software, 2020, 141, 102767.
21. Kong, Y., Pang, Z., Shao, H., Kolditz, O., "Optimization of well-doublet placement in geothermal reservoirs using numerical simulation and economic analysis", Environmental Earth Sciences, 2017, 76, 118.
22. Liang, X., Xu, T., Feng, B., Jiang, Z., "Optimization of heat extraction strategies in fault-controlled hydro-geothermal reservoirs", Energy, 2018, 164, 853-870.
23. Mahmoodpour, S., Singh, M., Turan, A., Bär, K., Sass, I., 2021a, Key parameters affecting the performance of fractured geothermal reservoirs: a sensitivity analysis by thermo-hydro-mechanical simulation, arXiv:2107.02277, [physics.geo-ph].
24. Mahmoodpour, S., Singh, M., Bär, K., Sass, I., 2021b, Thermo-hydro-mechanical modeling of an Enhanced geothermal system in a fractured reservoir using CO_2 as heat transmission fluid- A sensitivity investigation, arXiv:2108.05243 [physics.geo-ph].
25. Onwunalu, J.E., Durlofsky, L.J., "Application of a particle swarm optimization algorithm for determining optimum well location and type", Comput. Geosci., 2010, 14, 183–198.
26. Pandey, S.N., Singh, M., "Artificial neural network to predict the thermal drawdown of enhanced geothermal system", J. Energy Resour. Technol. 2021, 143(1):010901.
27. Samin, M.Y., Faramarzi, A., Jefferson, I., Harireche, O., "A hybrid optimization approach to improve long-term performance of enhanced geothermal system (EGS) reservoirs", Renewable Energy, 2019, 134, 379-389.
28. Sarma, P., Durlofsky, L.J., Aziz K., "Computational techniques for closed–loop reservoir modeling with application to a realistic reservoir", Petrol. Sci. Technol., 2008, 26, 1120–1140. 10th European Conference on the Mathematics of Oil Recovery.
29. Singh, M., Tangirala, S.K., Chaudhuri, A., "Potential of CO_2 based geothermal energy extraction from hot sedimentary and dry rock reservoirs, and enabling carbon geo-sequestration", Geom. Geop. Geo-Energy Geo-resour., 2020, 6, 16.
30. Stefansson, V., Geothermal reinjection experience, Geothermics, 1997, 26(1), 99-139.
31. Vaseghi, F., Ahmadi, M., Sharifi, M., Vanhoucke, M., "Generalized multi-scale stochastic reservoir opportunity index for enhanced well placement optimization under uncertainty in green and brownfields", Oil & Gas Science and Technology – Rev. IFP Energies Nouvelles, 2021, 76, 41.
32. Yousefzadeh, R., Sharifi, M., Rafiei, Y., "An efficient method for injection well location optimization using Fast Marching Method", Journal of Petroleum Science and Engineering, 2021, 204, 108620.
33. Zandvliet, M., Handels, M., Essen, G., Brouwer, R., Jansen, J., "Adjoint-based well-placement optimization under production constraints", SPE J., 2008, 13, 392–399.
34. Zhang, L., Deng, Z., Zhang, K., Long, T., Desbordes, J.K., Sun, H., Yang, Y., "Well-placement optimization in an enhanced geothermal system based on the fracture continuum method and 0-1 programming", Energies, 2019a, 12, 709.
35. Zhang, H., Huang, Z., Zhang, S., Yang, Z., Mclennan, J.D., "Improving heat extraction performance of an enhanced geothermal system utilizing cryogenic fracturing", Geothermics, 2020, 85, 101816.
36. Zhang, S., Jiang, Z., Zhang, S., Zhang, Q., Feng, G., "Well placement optimization for large-scale geothermal energy exploitation considering nature hydro-thermal processes in the Gonghe Basin, China", Journal of Cleaner Production, 2021, 317, 128391.
37. Zhang, W., Qu, Z., Guo, T., Wang, Z., "Study of the enhanced geothermal system (EGS) heat mining from variably fractured hot dry rock under thermal stress", Renewable Energy, 2019b, 143, 855-871.
38. COMSOL Multiphysics® v. 5.5. www.comsol.com. COMSOL AB, Stockholm, Sweden.